Characteristics of the Superconducting Field Winding of an HTS Wind Turbine Generator During a Short Circuit Fault

Dong Liu, *Member, IEEE*, Tiina Salmi, *Member, IEEE*, Fujin Deng, *Senior Member, IEEE*, and Changqing Ye

***Abstract*—High temperature superconducting generators (HTSGs) have great potential of high power density for future large direct-drive wind turbines. As synchronous machines, HTSGs have rapid rise of field currents during a sudden short circuit fault which cause AC losses in the HTS tapes. This paper applies *H-A* formulation of Maxwell equations for finite element simulation of electromagnetic behavior of a 10 MW, 9.6 rpm HTSGs. The model is integrated to a short circuit model to calculate the characteristics of the HTS field winding, such as field currents and AC losses during a three-phase no-load short circuit fault at the armature winding terminal. Two HTSG designs are compared. The n value characterizing the sharpness of the superconducting-resistive state transition of the HTS tape and the number of armature winding segments are analyzed as key variables. The result indicates high AC losses are produced but more armature winding segments can effectively reduce the AC loss and the field current. A lower n value can also lower the AC loss level but only for the non-magnetic rotor design. The field current is not affected by the n value for both HTSG designs.**

***Index Terms*—AC loss, H-formulation, HTS, short circuit, superconducting generator, wind turbine.**

I. Introduction

HIGH temperature superconducting generators (HTSGs) have great potential to be a high power density solution for future large direct-drive wind turbines. They will become quite competitive and then commercialized when the cost of HTS wires largely drops [1]–[4]. HTSGs are synchronous machines so they also possess the transient characteristics of synchronous machines during a sudden short circuit fault at the three-phase terminals. One essential characteristic is the rapid rise of field currents as illustrated in Fig. 1. Such rising of currents has no significant impact on copper conductors but challenges the safe operation of HTS materials. AC losses will then be produced as the increased current may approach or exceed the superconductor's critical current, leading to resistive losses in the superconductor or even a quench, where the superconducting state is completely suppressed. Moreover, the changing magnetic field generates AC losses in the superconductor, which in turn may generate heat and the critical current is further decreased as the temperature increases. The multi-physics analysis of AC losses is thus of pivotal importance in design of superconducting generators. Previous studies on transients characterization for HTSGs did not model the superconductivity, e.g. non-linear resistivity of the superconductor as shown in (1), but used a nearly-zero constant conductivity with only *A*-formulation [5]–[9]. Models that consider the non-linear resistivity need to be developed for transients study of HTSGs since the resistivity may limit the current rise but produce considerable AC losses that may cause temperature rise or damage the HTS winding.

This paper applies *H-A* formulation to model HTSGs for a 10 MW direct-drive wind turbine [10]–[13]. The model is integrated to a short circuit model to calculate the characteristics of the HTS field winding, such as field currents and AC losses during a three-phase short circuit fault. Two generator designs, namely fully iron-core (FIC) and non-magnetic rotor (NMR), as most considered in conceptual designs and demonstration projects are compared [14]–[19]. The n value of the non-linear resistivity of HTS tapes as given by (1) and the number of armature winding segments are analyzed as key variables.

Manuscript received September 29, 2021; revised November 27, 2021 and January 10, 2022; accepted January 18, 2022. Date of publication February 1, 2022; date of current version February 16, 2022. This work was supported in part by the Natural Science Foundation of Jiangsu Province of China under Grant BK20190486, in part by the Academy of Finland project (HiQuench) under Grant 336287, and in part by the Fundamental Research Funds for the Central Universities under Grant 2019B02914. *(Corresponding author: Dong Liu.)*

Dong Liu and Tiina Salmi are with the Unit of Electrical Enginerring, Tampere University, FI-33720 Tampere, Finland (e-mail: dong.liu@tuni.fi).

Fujin Deng is with the School of Electrical Engineering, Southeast University, Nanjing CN-210096, China.

Changqing Ye is with the College of Internet of Things Engineering, Hohai University, Changzhou 213022, China.

Color versions of one or more figures in this article are available at https://doi.org/10.1109/TASC.2022.3147427.

Digital Object Identifier 10.1109/TASC.2022.3147427

II. Modeling of HTSGs With *H-A* Formulation

An HTSG is modeled in two regions as sketched in Fig. 2. REBCO superconductors and their near air are modeled with *H*-formulation, and the rest is modeled with *A*-formulation. Thus, it is named *H-A* formulation.

A. H-Formulation

An HTSG has superconductors which feature a non-linear resistivity defined with the magnetic field and temperature dependent critical current density $J_c(B,T)$ by

$$\rho(J) = \rho_0 |J/J_c(B,T)|^{n-1} \tag{1}$$

$$\mu \partial_t \boldsymbol{H} + \nabla \times \boldsymbol{E} = 0 \tag{2}$$

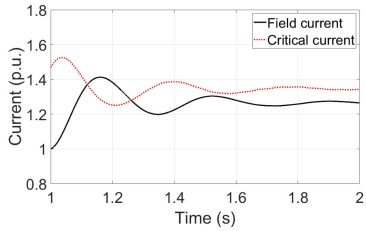

Fig. 1. Example of field currents during a short circuit of an HTSG [5]. The field winding is assumed always superconducting with no resistance during the short circuit. The critical current is calculated from the $J_c(B)$ curve of the superconducting tape at a fixed temperature.

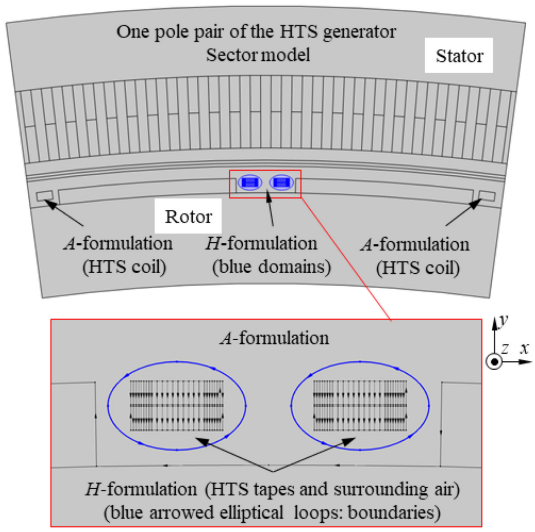

Fig. 2. Sketch of *H*- and *A*-formulation regions and their coupling boundaries in one pole pair. Only one pair of adjacent coil sides are modeled with *H*-formulation while the far coil sides are both modeled with *A*-formulation for calculating the induced voltage using the integral of E_z from (6). Top: Illustration of cross section of a pole pair of an HTSG. The armature windings are embedded in an iron structure external to the rotor with field coils made from HTS tapes. See Fig. 3 for the configurations. Bottom: Zoom-in view of the HTS coils modeled with *H*-formulation, in the form of sub-domains into which the HTS tapes are homogenized.

$$\boldsymbol{J} = \nabla \times \boldsymbol{H} \tag{3}$$

$$\boldsymbol{E} = \rho(J)\boldsymbol{J} \tag{4}$$

with $\rho_0 = E_c/J_c(B,T)$, $E_c = 1\mu$V/cm, μ is the permeability, and n is the power index defining the steepness of the current-voltage curve for characterizing a superconductor. Superconducting regions are formulated by the Faraday's law in (2) and the Ampere's law in (3). The electric field E is calculated from the current density J through the non-linear resistivity in (4). The term *H*-formulation means using directly the Maxwell's equations without any potential. The n value determines the resistivity of the HTS tape when J approaches or exceeds J_c. Different HTS tape production processes may result in a different n value. It is thus necessary to analyze the effects of the n value. In this paper, J_c is assumed fixed with varied n and its temperature dependence is neglected, meaning that J_c is only dependent on the magnetic flux density B.

B. A-Formulation

In the *A*-formulation, the Ampere's law with external currents is solved for the vector magnetic potential $\boldsymbol{A}$ defined by the flux density $\boldsymbol{B}$. The electric field $\boldsymbol{E}$ is obtained from $\boldsymbol{A}$ by applying the Stokes' theorem. The total current density $\boldsymbol{J}$ is the sum of the induced current density $\sigma\boldsymbol{E}$ and the external current density $\boldsymbol{J_e}$. The conductivity σ is a constant. Hence

$$\sigma\partial_t\boldsymbol{A} - \frac{1}{\mu}\nabla^2\boldsymbol{A} = \boldsymbol{J_e} \tag{5}$$

$$\boldsymbol{E} = -\partial_t\boldsymbol{A} \tag{6}$$

$$\boldsymbol{B} = \nabla \times \boldsymbol{A} \tag{7}$$

$$\boldsymbol{J} = \sigma\boldsymbol{E} + \boldsymbol{J_e} \tag{8}$$

C. Boundary Conditions

The coupling boundary between the *H*-formulation and *A*-formulation regions is shared by the two formulations. As we only need a two-dimensional model, the weak contribution (9) holds on this boundary in the *H*-formulation [20]. In the *A*-formulation, the weak contribution (10) holds instead. The tangential component of the magnetic field strength in the two formulations is defined by (11) using the field components in *H*-formulation, where t_x and t_y are the x and y components of the tangential vector $\boldsymbol{t}$, respectively, at a point on the boundary.

$$H\text{-formulation}: \quad E_z \cdot \text{test}(H_t^{(H)}) \tag{9}$$

$$A\text{-formulation}: \quad H_t^{(H)} \cdot \text{test}(A_z) \tag{10}$$

$$H_t^{(H)} = t_x \cdot H_x + t_y \cdot H_y \tag{11}$$

The weak contributions (9) and (10) are imposed in the two formulations, respectively, to couple their common boundaries. $H_t^{(H)}$ acts as the source for the *A*-formulation side of the boundary and $E_z = -\partial_t A_z$ acts as the source for the *H*-formulation side. The operator "test()" is to create test functions of a variable for the weak form of finite element methods. See [20] for an explanation of these boundary conditions.

D. Rotation

If the *H*-formulation is within the rotating rotor domains, which is the case in our generator model, the electric field E_z in (9) must be transformed to the rotating coordinate by

$$E_z = E_Z + \omega_m(X \cdot B_X + Y \cdot B_Y) \tag{12}$$

where the lowercase subscripts mean the coordinates of spatial type (x, y), the uppercase subscripts mean the coordinates of material type (X, Y), and ω_m is the angular frequency of the rotor rotation. The *H-A* formulation with rotating domains and the coordinate transformation are explained in detail in [20].

E. Current Density in H-Formulation

In *H*-formulation, external current densities cannot be applied to the superconductor tapes where the resistivity is non-linear. Thus, the wanted current density J_f should be applied to each

tape domain Ω of the HTS field winding using pointwise constraints as

$$J_f = \frac{1}{S}\int_{\Omega} J_z dS \tag{13}$$

F. AC Loss Calculation

The AC loss of each pole of the HTS field winding is calculated by

$$P_{ac} = l_s \int_{\Sigma\Omega} J_z \cdot E_z dS \tag{14}$$

where l_s is the axial stack length of the generator, and the end winding is assumed to be neglected.

G. Resistance of the HTS Fiend Winding

The resistance of the HTS field winding can be separated into two parts. One is the superconducting part r_{HTS} and the other is the current leads part r_{leads}. Hence

$$r_f = r_{\text{HTS}} + r_{\text{leads}} \tag{15}$$

The latter r_{leads} is constant, e.g. 20 mΩ, as an estimate from [21]. The former r_{HTS} contributes to all the AC loss so it can be calculated from the equality

$$i_f^2 r_{\text{HTS}} = l_s \int_{\Sigma\Omega} J_z \cdot E_z dS \tag{16}$$

where i_f is the field current, and l_s is the axial stack length of the generator.

H. Homogenization of the HTS Tapes

Homogenization is applied to the HTS tapes to speed up the computation. The multiple thin HTS tapes are homogenized into multiple subdomains. The tape is 12 mm wide and 0.2 mm thick. The number of subdomains is much lower than that of the HTS tapes, e.g. 25 subdomains vs. 153 tapes (FIC), 100 subdomains vs. 749 tapes (NMR). Each HTS coil has 153 (FIC) and 749 (NMR) HTS tapes, the cross-section of each coil side is divided to 25 and 100 subdomains, respectively. Each mesh element of the subdomain has a uniform current density. In [22], the homogenized model was concluded as a replacement of the original tape-based model to calculate current distribution and AC losses. For generators and motors where a cross section model is used for simulation, the electromagnetic transient behavior of the HTS coils can be calculated using the homogenized model without adding a big computational time load [22].

III. Generator Designs

Two HTSG designs are studied, both of which have an HTS field winding on the rotor (at 30 K) and copper armature windings on the stator (at 393 K). One is a fully iron-core (FIC) design (Fig. 3(a)) which saves the usage of costly HTS tapes but increases the weight. The other is a non-magnetic-rotor (NMR) design (Fig. 3(b)) where the rotor has no iron so as to reduce the weight but much more HTS tapes are needed to excite a high

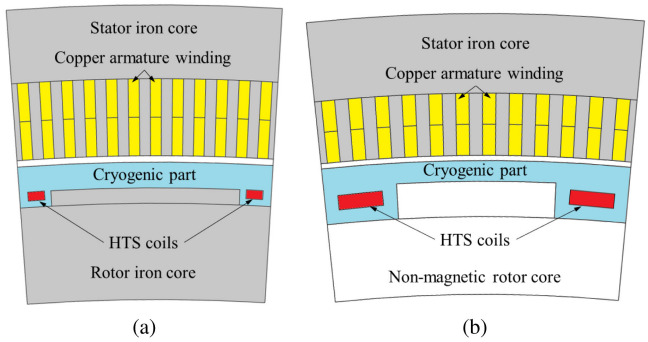

Fig. 3. One pole sketch of the HTSG. (a) FIC design. (b) NMR design.

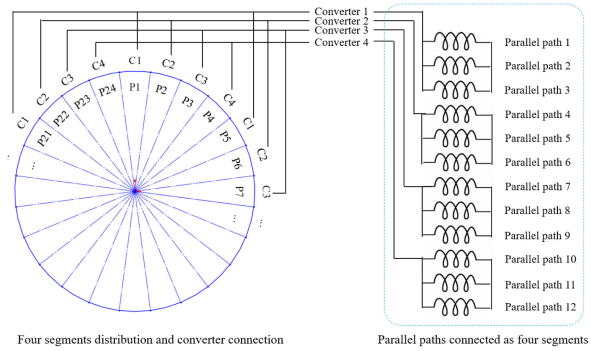

Fig. 4. Concept of multiple converters with four armature segments [6].

main magnetic field. The FIC design has 24 pole pairs while the NMR design has 16 pole pairs. Each HTS coil has two layers (one double-pancake) and four layers (two double-pancakes) for the FIC and NMR designs, respectively. To be used for a 10 MW, 9.6 rpm direct-drive wind turbine, the two generator designs have the same rated power of 11 MW, rated torque of 11 MNm, air gap diameter of 6 m, and axial stack length of 2.643 m. To achieve the same generator size, the cross-sectional area of the HTS coil of the NMR design is as large as 7 times that of the FIC design. The effective magnetic air gap, being the distance from the stator bore to the field winding, is fixed to 50 mm to accommodate the mechanical air gap, cryostat wall, vacuum chamber, and thermal insulations. The stator slot height is 120 mm in both designs. The stator slot fill factor is 0.5. The number of slots per pole per phase is 4. The RMS value of the rated stator winding current is 2.6 A/mm^2. Considering a 30% safety margin at normal operation, the rated field currents are 384 A/mm^2 and 369 A/mm^2 for the FIC and NMR designs, respectively.

When the power of wind turbines reaches 5 MW, it will not be wise to use a low-voltage power electronic converter (e.g. 690 V – 950 V) but a medium voltage converter (e.g. 3.3 kV). When the power reaches 10 MW, multiple converters may be used to avoid a single big converter which converts the full power and then each converter can be low-voltage. Each converter is connected to one segment of the generator's armature winding. The number of converters or segments is usually 2, 3 or 4. The topology of the converter and the armature segment is sketched in Fig. 4. Standard converters limit the low voltage ratings in

the range of 690 V to 950 V. Hence, the voltage rating can be 3.3 kV if only one big converter is used with the whole armature winding. Four segments of the armature winding will result in a rated voltage of 825 V. In this study, three armature winding segmentation scenarios are compared for each of the generator designs:

1) One full segment with rated voltage of 3.3 kV, being a medium-voltage option,

2) Two segments with rated voltage of 1150 V (which may not be practical but indicative for the comparative study), and

3) Four segments with rated voltage of 825 V, being a low-voltage option.

With more segments, the impact of short circuits of a one segment on the whole generator will be smaller and the probability of short circuits in more than one segments in the same time will become much lower [8].

IV. Modeling of Short Circuits

The generator's short circuit model is developed under the following simplifications and operation condition assumptions: i) The AC losses produced in the HTS field winding during the short circuit fault do not increase the temperature. This assumption will be checked in Section V-D. ii) The $J_c(B)$ curve and the resistivity of HTS tapes only consider the perpendicular component of the B-field, i.e. perpendicular with respect to the tape's wide face. iii) When the generator has multiple segments, the three-phase short circuit only occurs in one segment. iv) The rotational speed of the generator does not change during the short circuit fault. v) The electromagnetic shield is neglected. vi) Prior to the short circuit, the generator is under no-load rated-speed operation.

The phase currents i_a, i_b, i_c and the field current i_f are calculated from the following differential equations [23]:

$$[u_a, u_b, u_c] = \frac{\mathrm{d}[\lambda_a, \lambda_b, \lambda_c]}{\mathrm{d}t} - r_s[i_a, i_b, i_c] - L_{\sigma s}\frac{\mathrm{d}[i_a, i_b, i_c]}{\mathrm{d}t} \tag{17}$$

$$u_f = \frac{\mathrm{d}\lambda_f}{\mathrm{d}t} - r_f i_f - L_{\sigma f}\frac{\mathrm{d}i_f}{\mathrm{d}t} \tag{18}$$

where λ_a, λ_b and λ_c are the flux linkage of three phases, r_s and r_f are the winding resistances and $L_{\sigma s}$ and $L_{\sigma f}$ are the end winding inductances of the stator and field windings, respectively. The worse-case three-phase short circuit is simulated by forcing the phase voltages u_a, u_b and u_c to zero at $t = 0$ when the induced voltage of Phase A, $\mathrm{d}\lambda_a/\mathrm{d}t$, crosses zero. The field winding resistance r_f is calculated by (15).

V. Results

The characteristics of the HTS field winding, i.e. field currents, AC losses, are calculated with COMSOL Multiphysics using the above-mentioned *H-A* formulation and finite element models. The results contain data of five time periods.

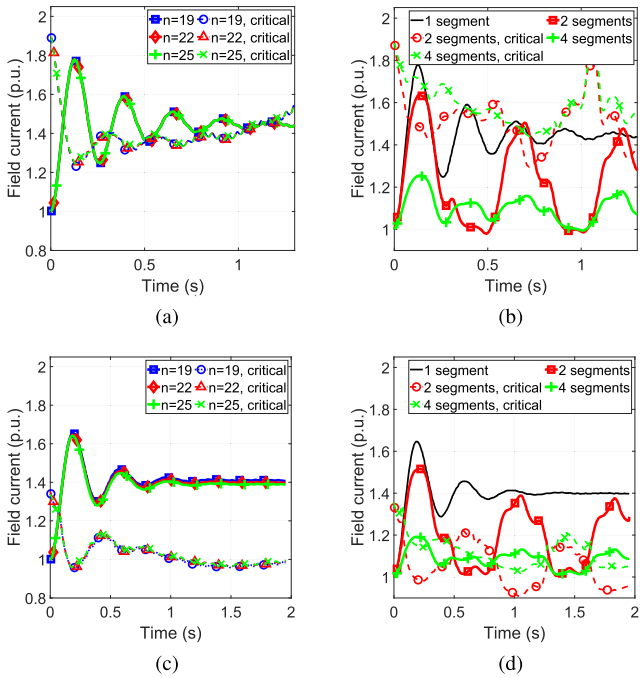

Fig. 5. Field currents and critical currents during the three-phase short circuit. (a) Varying n 1 segment, FIC design. (b) Segmented, $n = 22$, FIC design. (c) Varying n, 1 segment, NMR design. (d) Segmented, $n = 22$, NMR design.

A. Field Currents

The variation of the n-value in the range between 19 and 25 does not have a significant impact on the field current i_f during the short circuit, as shown in Fig. 5. This is mainly because the total resistance of the field winding is low compared to the high leakage reactance ($X_{\sigma f} = 145\,\Omega$ for the FIC design and $X_{\sigma f} = 164\,\Omega$ for the NMR design) although the HTS resistance has significantly increased (see Section V-C). The field current exceeds the critical current shortly after the short circuit starts. Then, the field current is hardly below the critical current in both designs. The FIC generator design has a slightly higher peak field current than the NMR design. More segments of the armature winding effectively reduce the field current but lead to larger ripples. The large ripples are caused by the field poles on the rotor periodically passing by the short-circuited segment of the armature winding on the stator. More segments also effectively reduce the duration when the field current exceeds the critical current, which results in a lower AC loss level as shown in Fig. 6.

B. AC Losses

The n value hardly changes the AC loss level P_{ac} of the FIC generator design but significantly affect that of the NMR design, as shown in Fig 6. With the original $n = 22$, the AC loss level of the FIC design is only 1/12 that of the NMR design. This is mainly because the varying magnetic field is highly confined in the iron near the HTS coils for the FIC design but extensively exist in the HTS tapes of the NMR design. The total AC losses of both designs are as high as MW levels but the high AC losses do not persist long (shorter than one period). Such AC loss levels may challenge the cryogenic cooling designed only for normal

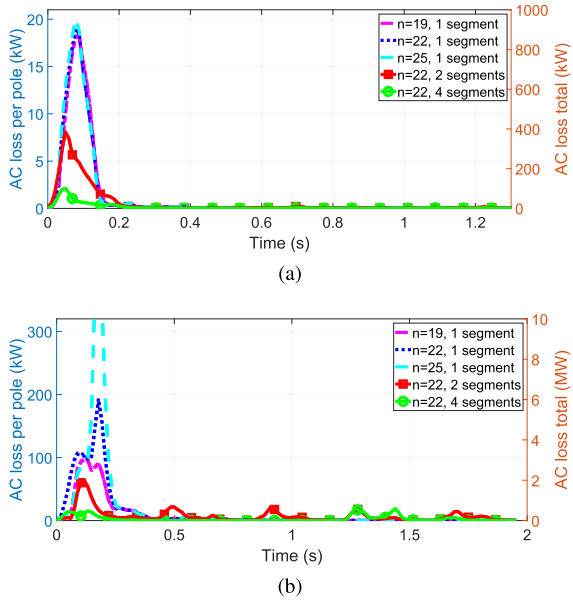

Fig. 6. AC losses during the three-phase short circuit for different n values and different numbers of segments. (a) FIC design. (b) NMR design.

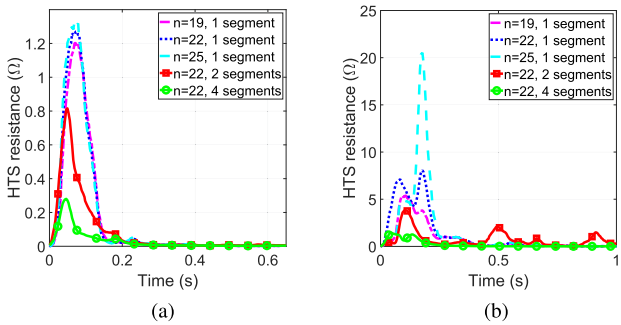

Fig. 7. Resistance of the superconducting part of the HTS field winding during the three-phase short circuit for different n values and different numbers of segments. (a) FIC design. (b) NMR design.

operation. More segments effectively reduce the AC loss level for both designs. Then the total AC loss level may not be too challenging especially for the FIC design.

C. Resistance of the Superconducting Part

As shown in Fig. 7, the resistance of the superconducting part of the HTS field winding r_{HTS} follows a similar characteristic to the AC losses in Fig. 6 due to the relationship in (16). The absolute value of the HTS resistance is quite low so that adding it to the field winding resistance cannot reduce the field current during the short circuit fault. As a reference, the current leads have a resistance of 20 mΩ. However, these results are obtained with the assumption that the AC loss does not increase the temperature which will lead to further increase of resistance. If a thermal model is included, the resistance level may be different.

D. Discussion

The rise of the field current may cause the current over the critical current. For both designs with $n = 22$ and without

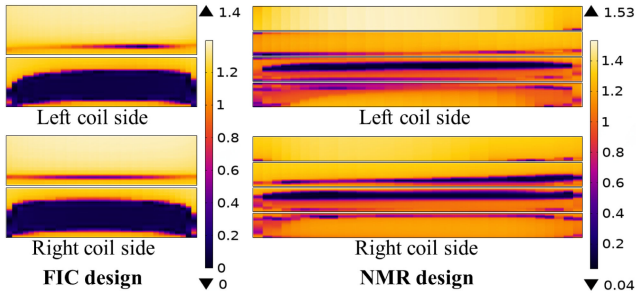

Fig. 8. Surface plots of the absolute ratio of field currents to critical currents (J/J_c) when it is maximum during the short circuit. Coil sizes of both designs are not under the same scale.

segmentation, the absolute ratio of the current density to the critical current density (J/J_c) in the HTS coils is calculated. The distribution of the ratio is plotted in Fig. 8 when the ratio reaches it maximum during the short circuit. The majority of the coil has a current density J near or over the critical current density J_c but the excess is not much, e.g. max. 1.4 for the FIC design and 1.53 for the NMR design. This over-current may cause temperature rise due to the increase of resistivity during the transition from the superconducting state to the normal state.

The temperature rise is checked with an analytic adiabatic model for both designs with $n = 22$ and without segmentation. This model uses the specific heat of the materials in the HTS tape and the deposited volumetric energy due to the AC losses. The energy is assumed uniformly distributed in the HTS coil, which limits the accuracy of the model but enables rapid check without a detailed thermal model. The calculated temperature rises are 3.9 K and 8.4 K, respectively for the FIC and NMR designs, based on the operation temperature of 30 K. The temperature rises are not as high as the AC loss magnitudes imply. The most probable reason is that the AC-loss energy built up mainly in the first period is low, and the volume of the field winding is sufficiently large. This simple check also confirms that the NMR design is more challenging regarding cooling of the AC losses. However, the temperature rise will cause J_c to drop and then the resistivity of the HTS tape (r_{HTS}) to further increase (compared with Fig. 7). This effect may then limit the rise of the field current during the short circuit. A thermal model, which is more accurate than the analytic adiabatic model, is needed to be integrated to the current short circuit model. Then, the time-dependent temperature rise will be calculated and, iteratively, the increasing resistivity r_f will influence the field current i_f in (18).

VI. Conclusion

A short circuit model of HTSGs has been developed using *H-A* formulation. The characteristics of the field winding of two HTSG designs, i.e. fully iron-core (FIC) design and non-magnetic-rotor (NMR) design, during a three-phase short circuit fault are obtained by applying the developed short circuit model. The n value of the HTS tape drastically affects the field current for the NMR design. AC loss levels have been found high. Dividing the armature winding into multiple segments effectively reduces the field current and the AC loss in the HTS

field winding when only one segment is shorted. In practice, offshore wind turbines over 10 MW have already implemented multiple armature segments. Thus, the transient AC loss may not cause a sufficiently high energy deposited per unit volume or significant increase the temperature. Choosing an HTS tape with a low n value also helps lowering the AC loss level for the NMR generator design but does not work for the FIC generator design. A lower n may cause a different $J_c(B)$ curve. In future work, the effects of $J_c(B)$ curves will be studied as well.

The resistance of the superconducting part of the HTS field winding rises during the transient. The model in the paper assumes that the AC loss does not heat up the HTS field winding. A rapid analytical adiabatic check estimates that the temperature rises by a few Kelvins so this assumption can be considered valid. In future work, a detailed thermal model will be integrated into the present model, thereby enabling calculation of the temperature distribution, HTS resistivity distribution, and temperature-dependent field current during the short circuit.

REFERENCES

[1] K. S. Haran *et al.*, "High power density superconducting rotating machines-development status and technology roadmap," *Supercond. Sci. Technol.*, vol. 30, 2017, Art. no. 123002.

[2] B. B. Jensen, N. Mijatovic, and A. B. Abrahamsen, "Development of superconducting wind turbine generators," *J. Renewable Sustain. Energy*, vol. 5, 2013, Art. no. 023137.

[3] H. Polinder, J. A. Ferreira, B. B. Jensen, A. B. Abrahamsen, K. Atallah, and R. A. McMahon, "Trends in wind turbine generator systems," *IEEE J. Emerg. Sel. Top. Power Electron.*, vol. 1, no. 3, pp. 174–185, Sep. 2013.

[4] D. Liu, H. Polinder, A. B. Abrahamsen, and J. A. Ferreira, "Potential of partially superconducting generators for large direct-drive wind turbines," *IEEE Trans. Appl. Supercond.*, vol. 27, no. 5, Aug. 2017, Art. no. 5203711.

[5] X. Song, D. Liu, H. Polinder, N. Mijatovic, J. Holbøll, and B. B. Jensen, "Short circuit of a 10-MW high-temperature superconducting wind turbine generator," *IEEE Trans. Appl. Supercond.*, vol. 27, no. 4, Jun. 2017, Art. no. 5201505.

[6] X. Song, Y. Wang, D. Liu, S. Wang, and D. Liang, "Short-circuit characteristics of a high temperature superconducting wind turbine generator employing a segmented armature winding," *IEEE Trans. Appl. Supercond.*, vol. 29, no. 5, Aug. 2019, Art. no. 5202605.

[7] S. J. Jung *et al.*, "Stator winding fault influence on the field coil of a 10 MW superconducting synchronous generator," *IEEE Trans. Appl. Supercond.*, vol. 23, no. 3, Jun. 2013, Art. no. 5200104.

[8] Y. Liu, R. Qu, J. Wang, H. Fang, X. Zhang, and H. Chen, "Influences of generator parameters on fault current and torque in a large-scale superconducting wind generator," *IEEE Trans. Appl. Supercond.*, vol. 25, no. 6, Dec. 2015, Art. no. 5204309.

[9] Z. Huang, A. Zhao, X. Huang, B. Zhu, Y. Jiang, and Z. Jin, "Short-circuit fault simulations in an HTS wind generator with different mechanical conditions," *IEEE Trans. Appl. Supercond.*, vol. 28, no. 3, Apr. 2018, Art. no. 5204606.

[10] B. Shen, F. Grilli, and T. Coombs, "Review of the AC loss computation for HTS using H formulation," *Supercond. Sci. Technol.*, vol. 33, no. 3, 2020, Art. no. 033002.

[11] F. Grilli *et al.*, "Electromagnetic modeling of superconductors with commercial software: Possibilities with two vector potential-based formulations," *IEEE Trans. Appl. Supercond.*, vol. 31, no. 1, Jan. 2021, Art. no. 5900109.

[12] C. R. Vargas-Llanos, S. Lengsfeld, and F. Grilli, "T-A formulation for the design and AC loss calculation of a superconducting generator for a 10 MW wind turbine," *IEEE Access*, vol. 8, pp. 208767–208778, 2020.

[13] L. Bortot *et al.*, "A coupled A-H formulation for magneto-thermal transients in high-temperature superconducting magnets," *IEEE Trans. Appl. Supercond.*, vol. 30, no. 5, Aug. 2020, Art. no. 4900911.

[14] D. Liu, H. Polinder, A. B. Abrahamsen, and J. A. Ferreira, "Topology comparison of superconducting generators for 10-MW direct-drive wind turbines: Cost of energy based," *IEEE Trans. Appl. Supercond.*, vol. 27, no. 4, Jun. 2017, Art. no. 5202007.

[15] R. Fair *et al.*, "Superconductivity for large scale wind turbines," United States: N. p., 2012. Web. doi: 10.2172/1052970.

[16] X. Song *et al.*, "Designing and basic experimental validation of the world's first MW-class direct-drive superconducting wind turbine generator," *IEEE Trans. Energy Convers.*, vol. 34, no. 4, pp. 2218–2225, Dec. 2019.

[17] X. Song *et al.*, "Commissioning of the world's first full-scale MW-class superconducting generator on a direct drive wind turbine," *IEEE Trans. Energy Convers.*, vol. 35, no. 3, pp. 1697–1704, Sep. 2020.

[18] X. Song *et al.*, "Ground testing of the world's first MW-class direct-drive superconducting wind turbine generator," *IEEE Trans. Energy Convers.*, vol. 35, no. 2, pp. 757–764, Jun. 2020.

[19] X. Song *et al.*, "Experimental validation of a full-size pole pair set-up of an MW-class direct drive superconducting wind turbine generator," *IEEE Trans. Energy Convers.*, vol. 35, no. 2, pp. 1120–1128, Jun. 2020.

[20] R. Brambilla, F. Grilli, L. Martini, M. Bocchi, and G. Angeli, "A finite-element method framework for modeling rotating machines with superconducting windings," *IEEE Trans. Appl. Supercond.*, vol. 28, no. 5, Aug. 2018, Art. no. 5207511.

[21] S. S. Kalsi, "Rotating AC machines," in *Applications of High Temperature Superconductors to Electric Power Equipment*, Hoboken, NJ, USA: Wiley, 2011, pp. 59–128.

[22] V. Zermeno *et al.*, "Calculation of alternating current losses in stacks and coils made of second generation high temperature superconducting tapes for large scale applications," *J. Appl. Phys*. vol. 114, no 17, 2013, Art. no. 173901.

[23] S. Umans, "Transient performance of a high-temperature-superconducting generator," in *Proc. Electric Mach. Drives Conf.*, 2009, pp. 451–457.